Journal of Materials Chemistry A

PAPER

View Article Online
View Journal | View Issue

Cite this: J. Mater. Chem. A, 2015, 3, 21244

Novel 3DOM $BiVO_4/TiO_2$ nanocomposites for highly enhanced photocatalytic activity†

Meryam Zalfani,‡[ab] Benoit van der Schueren,‡[a] Zhi-Yi Hu,‡[c] Joanna C. Rooke,[a] Ramzi Bourguiga,[b] Min Wu,*[d] Yu Li,*[d] Gustaaf Van Tendeloo[c] and Bao-Lian Su*[ade]

Novel 3DOM $BiVO_4/TiO_2$ nanocomposites with intimate contact were for the first time synthesized by a hydrothermal method in order to elucidate their visible-light-driven photocatalytic performances. $BiVO_4$ nanoparticles and 3DOM TiO_2 inverse opal were fabricated respectively. These materials were characterized by XRD, XPS, SEM, TEM, N_2 adsorption–desorption and UV-vis diffuse (UV-vis) and photoluminescence spectroscopies. As references for comparison, a physical mixture of $BiVO_4$ nanoparticles and 3DOM TiO_2 inverse opal powder (0.08 : 1), and a $BiVO_4$/P25 TiO_2 (0.08 : 1) nanocomposite made also by the hydrothermal method were prepared. The photocatalytic performance of all the prepared materials was evaluated by the degradation of rhodamine B (RhB) as a model pollutant molecule under visible light irradiation. The highly ordered 3D macroporous inverse opal structure can provide more active surface areas and increased mass transfer because of its highly accessible 3D porosity. The results show that 3DOM $BiVO_4/TiO_2$ nanocomposites possess a highly prolonged lifetime and increased separation of visible light generated charges and extraordinarily high photocatalytic activity. Owing to the intimate contact between $BiVO_4$ and large surface area 3DOM TiO_2, the photogenerated high energy charges can be easily transferred from $BiVO_4$ to the 3DOM TiO_2 support. $BiVO_4$ nanoparticles in the 3DOM TiO_2 inverse opal structure act thus as a sensitizer to absorb visible light and to transfer efficiently high energy electrons to TiO_2 to ensure long lifetime of the photogenerated charges and keep them well separated, owing to the direct bandgap of $BiVO_4$ of 2.4 eV, favourably positioned band edges, very low recombination rate of electron–hole pairs and stability when coupled with photocatalysts, explaining the extraordinarily high photocatalytic performance of 3DOM $BiVO_4/TiO_2$ nanocomposites. It is found that larger the amount of $BiVO_4$ in the nanocomposite, longer the duration of photogenerated charge separation and higher the photocatalytic activity. This work can shed light on the development of novel visible light responsive nanomaterials for efficient solar energy utilisation by the intimate combination of an inorganic light sensitizing nanoparticle with an inverse opal structure with high diffusion efficiency and high accessible surface area.

Received 30th January 2015
Accepted 8th September 2015

DOI: 10.1039/c5ta00783f

www.rsc.org/MaterialsA

1. Introduction

In recent years, semiconductor photocatalysts have attracted a great deal of attention due to their potential application in environmental remediation. Among these semiconductors, TiO_2 has been extensively investigated as the most promising photocatalyst because of its safety, low-cost and high efficiency under UV light irradiation.[1] However, the broad bandgap energy of this metal oxide limits its use in visible light[2] as TiO_2 is active only under ultraviolet (UV) light, about 3–5% of the solar spectrum. In addition, the low rate of electron transfer to oxygen and a high recombination rate of photogenerated electron–hole pairs result in its low photo-quantum efficiency.[3–5] Many strategies have been developed to improve the photocatalytic efficiency of TiO_2 through second component doping to promote the photon to electron conversion efficiency, photogenerated charge separation and visible light harvesting. The combination of TiO_2 with a sensitizer semiconductor system has shown superior performance such as enhanced or tuneable light absorption within TiO_2, improved photo-generated electron–hole separation and exalted interfacial charge transfer

[a]Laboratory of Inorganic Materials Chemistry (CMI), University of Namur (UNamur), 61 rue de Bruxelles, B-5000 Namur, Belgium. E-mail: bao-lian.su@unamur.be
[b]Laboratoire de Physique des Matériaux: Structure et Propriétés, Groupe Physique des Composants et Dispositifs Nanométriques, Faculté des Sciences de Bizerte, University of Carthage, 7021 Jarzouna-Bizerte, Tunisia
[c]EMAT (Electron Microscopy for Materials Science), University of Antwerp, Groenenborgerlaan 171, B-2020 Antwerp, Belgium
[d]State Key Laboratory of Advanced Technology for Materials Synthesis and Processing, Wuhan University of Technology, Luoshi Road 122, 430070, Wuhan, Hubei, China. E-mail: minwu@whut.edu.cn; baoliansu@whut.edu.cn
[e]Department of Chemistry and Clare Hall College, University of Cambridge, Lensfield Road, Cambridge, United Kingdom. E-mail: bls26@cam.ac.uk

† Electronic supplementary information (ESI) available. See DOI: 10.1039/c5ta00783f

‡ The authors contributed equally to this work.

efficiency.[6] Coupling narrow-bandgap semiconductors such as CdS (ref. 7) and $CuBi_2O_4$ (ref. 8) with wide-bandgap semiconductors like TiO_2, SnO_2 (ref. 9) and WO_3 (ref. 10) and forming composite photocatalysts such as Bi_2WO_6/TiO_2, Bi_2O_3/TiO_2, In_2O_3/TiO_2, Cu_2O/TiO_2, WO_3/TiO_2, *etc.* have been extensively investigated.[11–15] Ke *et al.*[16] showed that WO_3/TiO_2 nanocomposites present much higher photocatalytic activity than pure TiO_2 in the photodegradation reaction of rhodamine B (RhB) under UV light. Vinodgopal *et al.*[17] studied a coupled SnO_2/TiO_2 semiconductor system which carried out a very rapid and complete decolorization of the textile azo dye under UV irradiation. Bessekhouad *et al.*[18] reported that a Bi_2O_3/TiO_2 heterojunction structure presented higher activity than pure Bi_2O_3 and TiO_2-P25 for the photocatalytic degradation of Orange II under UV-vis irradiation.

The monoclinic $BiVO_4$ structure was reported to show highly promising photocatalytic activity under visible light irradiation due to its relatively narrow bandgap energy of 2.4 eV, compared to its two tetragonal phases both with a bandgap energy of 3.1 eV.[19–21] Due to its visible light photocatalytic activity, it has also been used for the degradation of organic pollutants and oxygen evolution in the water splitting reaction.[22,23] The combination of a narrow bandgap semiconductor material such as $BiVO_4$ with TiO_2 to produce a $BiVO_4/TiO_2$ nanocomposite with an intimate heterojunction could be an efficient way to offer a visible light photocatalyst with high photocatalytic activity and attracts increasing attention.[20,24–30] Cao *et al.*[24] synthesized the porous peanut-like $BiVO_4/TiO_2$ composite nanostructures by a hydrothermal process and the photocatalytic activity of these $BiVO_4/TiO_2$ nanostructures was largely enhanced. Zhang *et al.*[25] reported the synthesis of $BiVO_4/TiO_2$ by a one-step microwave hydrothermal method and found that the 20 wt% $TiO_2/BiVO_4$ nanocomposite exhibited better photocatalytic activity than pure monoclinic $BiVO_4$ and other percentages of TiO_2 in $BiVO_4$ because of its high crystallinity, narrow bandgap, and most importantly, the hierarchical heterostructure which can effectively separate photoinduced electron–hole pairs on the surface of $BiVO_4/TiO_2$ photocatalysts. They claimed that $BiVO_4$ played the role of a light sensitizer. The sensitizer effect of $BiVO_4$ has also been pointed out by Tang *et al.*[30] Colon *et al.*[20,31] studied a ternary erbium doped $BiVO_4/TiO_2$ heterostructure made by a simple impregnation method which showed highly enhanced photocatalytic activity in the degradation of phenol[20] and methylene blue.[31] They attributed this high photocatalytic activity of erbium doped $BiVO_4/TiO_2$ to the occurrence of a luminescence process generated by erbium ions and the possibility to adjust the band position between Er^{3+} doped $BiVO_4$ and TiO_2, leading to the effective charge pair separation. Hu *et al.*[26] prepared $BiVO_4/TiO_2$ with a mass ratio of 1 : 200 by hydrothermal treatment for the benzene degradation reaction and claimed that their material was 3–4 times more active than nitrogen doped TiO_2 under visible light irradiation. A bilayer TiO_2 photonic crystal (PC)/porous $BiVO_4$ was constructed by using liquid-phase deposition and spin coating by Huo *et al.*[32] The photocatalytic ability of porous $BiVO_4$ was enhanced by combination with a TiO_2 PC layer as the back reflector which intensified the light absorbance, showing another advantage of a TiO_2 PC crystal in enhancing light absorption and the combination of $BiVO_4$ and TiO_2. In spite of these promising results, the role of $BiVO_4$ in $BiVO_4/TiO_2$ heterostructures and the photoelectronic mechanism remain a point of debate. Moreover, the accessibility of reactants to these heterostructures is not favourable due to the low porosity, low surface area of TiO_2 supports and poor adsorptive properties of $BiVO_4$.[21,33] Xie *et al.*[29] in their recent paper showed very clearly the importance of the combination of TiO_2 and $BiVO_4$ to achieve long life visible light excited charge carriers which gave unexpectedly high photocatalytic activity for water splitting. Pure Mo doped $BiVO_4$ inverse opal structures were prepared.[34] Due to the specific structure, higher photocurrent density owing to effective charge collection was observed leading to an enhancement in photoelectrochemical water splitting and showing the importance of the macroporous inverse opal structure in charge collection.

The photocatalytic behaviour of highly ordered three dimensional macroporous titania with an inverse opal structure and good accessibility of reactants in dye molecule degradation has been investigated.[35–40] Wu *et al.*[35] studied the degradation of RhB with a 3DOM TiO_2 inverse opal structure with different pore diameters. They have shown that the photocatalytic activity presents a variation with the pore diameter. In this framework, Zheng *et al.*[36] demonstrated that the order of benzoic acid (BA), methyl orange (MO) and RhB photocatalytic degradation is related to the pore size of the TiO_2 inverse opal structure (IOS). With the increasing pore size of the TiO_2 IOS, mass transfer and light utilization efficiency are enhanced. The continuous pore voids facilitate the transfer of reactant molecules which is beneficial for dye sensitization.

On the other side, since 3DOM inverse opal structures as photonic crystals (PCs) have periodic dielectric contrast modulation in the length scale of the wavelength of light, coherent Bragg diffraction forbids light with certain energies to propagate through the material along a particular crystallographic direction. This gives rise to stop-band reflection, and the range of energies that is reflected back depends on the periodicity and dielectric contrast of the PC. At the wavelengths corresponding to the edges of these stop-bands, photons propagate with strongly reduced group velocity and hence are called 'slow photons'. The slow photons can be used to enhance the light absorption of materials when the photon energy matches the absorbance of the material leading to the generation of a large number of electron–hole pairs and enhanced photocatalytic activity. Liu *et al.*[38–40] investigated the slow photon effect on the photocatalytic activity of inverse opal ZnO by tuning the incident light angle.[38–40] Compared with bulk ZnO, it was found that inverse opal ZnO exhibits much higher photocatalytic activity.

Chen *et al.*[41] have also demonstrated that inverse opal WO_3 photoanodes with different stop-bands showed enhanced photocurrent intensity. Photonic crystals, particularly titania, have been considered as components in dye-sensitized photoelectrochemical cells designed to increase the efficiency of the solar cells by enhancing photocurrent efficiencies due to the localization of heavy photons near the edges of photonic gaps.[42–46] The slow photon effect on photovoltaic cells and the photochemical process was investigated by Nishimura *et al.*[46] and Chen *et al.*[47–49] as a means of promoting the optical

absorbance of the TiO_2 based composite system. In addition to this slow photon effect, the 3DOM structure has an open interconnected porous network, facilitating the diffusion of molecules and offering a larger surface area, both being quite favourable for photocatalysis.[50,51]

In order to benefit from the advantages of both the composite system and the 3DOM structure, we have combined the 3DOM TiO_2 with the narrow bandgap semiconductor $BiVO_4$ as a light sensitizer leading to visible light absorbing materials with enhanced photocatalytic activity. To the best of our knowledge, we have for the first time prepared 3DOM $BiVO_4/TiO_2$ nanocomposites offering a heterojunction by their intimate contact. In this work, the synthesis, characterization, and photocatalytic activity of 3DOM $BiVO_4/TiO_2$ nanocomposites in the visible light degradation of a dye molecular model were studied. The mechanism of enhanced visible light photocatalytic activity of the as-synthesized nanocomposites is proposed and discussed. For comparison, TiO_2 inverse opal, $BiVO_4$ nanoparticles, a physical mixture of $BiVO_4$ nanoparticles and 3DOM TiO_2 powders, and the $BiVO_4$/P25 TiO_2 nanocomposite by a hydrothermal method were synthesized and used as references.

2. Experimental

2.1 Synthesis of 3DOM TiO_2, $BiVO_4$ and 3DOM $TiO_2/BiVO_4$ nanocomposites

Styrene, sodium hydroxide and potassium persulfate were purchased from Aldrich. Polystyrene (PS) spheres were synthesized by an emulsion polymerization method without the addition of a surfactant. Styrene (20 mL) was washed three times with a solution of NaOH (1 M) to remove the polymerization inhibitor, and then added to 160 mL of bidistilled water in a two-neck flask. This solution was stirred at 350 rpm under an inert atmosphere and heated to 70 °C. After 30 min and when the temperature was stabilised at 70 °C, 0.16 g of $K_2S_2O_8$ was added to initiate polymerization. After 30 min, the mixture became cloudy and after 6 hours the polymerization was stopped by cooling and venting the flask. The white solution obtained was a dispersion of PS beads in water. The PS sphere size was around 350 nm.

To obtain an opal structured template, the PS beads dispersion was self-assembled by oven-drying at 40 °C for 5 days and characterised by scanning electron microscopy (SEM).

The fabrication of three dimensionally ordered macroporous (3DOM) titania was achieved *via* a templating strategy, as reported in the literature,[35,38–40,52,53] in which a thick layer of self-assembled polystyrene spheres (PS) was deposited onto a filter paper in a Buchner funnel under vacuum. The PS assembly was then infiltrated with the precursor solution. Titanium isopropoxide (Aldrich, 97%) was added dropwise to completely cover the PS spheres whilst under vacuum such that it occupied the voids inside the PS assembly. The precursor–template mixture was then air dried for 24 h and subsequently calcined at 550 °C for 12 h at a heating rate of 2 °C min^{-1} to obtain TiO_2 photonic crystals (PCs) with an inverse opal structure (IOS). In order to incorporate $BiVO_4$ nanoparticles inside the voids of the 3DOM TiO_2, a hydrothermal method was used. In a typical process, stoichiometric amounts of $Bi(NO_3)_3 \cdot 5H_2O$ (Carl Roth, ≥98%, p.a. ACS) and NH_4VO_3 (Carl Roth, ≥98%, p.a.) were dissolved in a stoichiometric volume of an ethylene glycol–water mixture and stirred for about 10 min until a clear solution was formed. Then, different amounts of 3DOM TiO_2 were added into the solution and sonicated for 15 min. After 1 h stirring, the obtained yellow-coloured mixture was transferred into a Teflon-sealed autoclave which was maintained at 160 °C for 24 h. The solid powders were recovered by centrifugation and washed with distilled water and absolute ethanol three times. Finally, the obtained solid was vacuum-dried at 60 °C for 6 h and was then calcined at 300 °C for 1 h. Dumbbell-like $BiVO_4$ structures were synthesized under the same experimental conditions. Two other reference samples were prepared for comparison of photocatalysis. Firstly, $BiVO_4$ nanoparticles were introduced into P25 TiO_2 nanoparticles by the same method described above by hydrothermal synthesis. After washing, the sample recovered was labelled as the $BiVO_4$/P25-TiO_2 nanocomposite. Secondly, the obtained $BiVO_4$ dumbbell-like structure was mixed with 3DOM TiO_2 inverse opal powders, giving a physical mixture of $BiVO_4$ and 3DOM TiO_2, labelled as phy-mix $BiVO_4$/3DOM TiO_2 IO.

2.2 Material characterisation

Powder X-ray diffraction was performed on a PANalytical X'pert Pro with Cu Kα radiation. Textural properties of the materials were evaluated *via* adsorption–desorption of nitrogen at −196 °C using a Micromeritics Tristar 3000 with prior outgassing. The morphological properties of the samples were observed by scanning electron microscopy (SEM) (FEI FEI Helios Nanolab 650). Furthermore, transmission electron microscopy (TEM), scanning transmission electron microscopy (STEM), and Energy Dispersive X-ray spectroscopy (EDX) were performed on a FEI Tecnai Osiris electron microscope fitted with Super-X windowless EDX detector system, operated at 200 kV. X-ray photoelectron spectroscopy (XPS) analysis was performed on a K-Alpha™ + X-ray photoelectron spectrometer (XPS). The binding energy for the C (1s) peak at 284.9 eV (relative to adventitious carbon from the XPS instrument itself) was used as a reference. The UV-vis absorbance spectra were obtained using a UV-vis spectrophotometer (Perkin Elmer Lambda 35 UV-visible spectrometer fitted with a Labsphere for analysis in diffuse reflectance mode) in the range of 200–750 nm. Photoluminescence properties of the samples were studied by Perkin Elmer LS45 luminescence spectrometry.

2.3 Photocatalytic testing

Photocatalytic testing was performed under visible light irradiation (400–800 nm) using 6 neon lamps of 18 W. The luminous power of each lamp was 1250 lm and the total luminous power was 7500 lm in the photocatalytic reactor. The emission spectrum of the neon light lamp is given in Fig. 1S.† It can be seen that the intensity of UV light emitted by the neon lamp was very low and can be neglected, and hence no UV filter was used to cut the UV light. The reaction temperature was maintained at room temperature. In each experiment 20 mg of the photocatalyst was placed in 50 mL of reactant solution with an initial

concentration of 10^{-3} M of RhB. The suspension was poured into a quartz tube, inserted into a reactor and stirred in the dark for 120 min to ensure adsorption/desorption equilibrium prior to irradiation. During irradiation, 2 mL of the suspension was removed at a given time interval for subsequent RhB concentration analysis.

3. Results and discussions

3.1 Phase composition

XRD patterns of the as-prepared 3DOM TiO_2 inverse opal, two $BiVO_4$/3DOM TiO_2 nanocomposites and $BiVO_4$ nanoparticles are shown in Fig. 1. The XRD pattern (Fig. 1a) of the TiO_2 inverse opal structure shows five peaks at $2\theta = 25.3°$, 37.9°, 48.0°, 54.6° and 62.8° corresponding to the crystal planes of (101), (004), (200), (211), and (204), respectively (JCPDS card no. 14-0688), which indicates that the TiO_2 sample adopts an anatase phase after calcination at 550 °C. The XRD peaks (Fig. 1d) of $BiVO_4$ nanoparticles correspond to the monoclinic scheelite phase (JCPDS 14-0688). The diffraction profiles reveal that both $BiVO_4$ and TiO_2 powder are highly crystalline. The diffraction patterns of $BiVO_4$/3DOM TiO_2 nanocomposites (Fig. 1b and c) showed the combination of the XRD profiles of both TiO_2 inverse opal and $BiVO_4$ nanoparticles. Weak XRD diffraction peaks of vanadate species at $2\theta = 18.8°$, 28.8°, 30.5°, 35°, 39.9° and 42.4° corresponding to the crystal planes of (011), (121), (040), (002), (−1,1,2) and (150), respectively, are observed as shown by (■) in Fig. 1b and c. This is presumably due to a combination of their low content and high dispersion.

The average crystallite sizes of pure $BiVO_4$ nanoparticles, pure TiO_2 inverse opal structure and TiO_2 nanoparticles in the 0.08$BiVO_4$/3DOM TiO_2 nanocomposite, calculated by the Scherrer equation, were found to be 30.0, 29.4 and 22.5 nm, respectively. In general, an increase of the crystallite size is observed in the high temperature treated samples. However, the TiO_2 crystallite size decreases in the $BiVO_4$/TiO_2 nanojunction composites compared to that in pure TiO_2 inverse opal, which is confirmed by the presence of broad peaks in the diffraction pattern of the 0.08$BiVO_4$/3DOM TiO_2 nanocomposite. This can be ascribed to the fact that the introduced $BiVO_4$ nanoparticles inhibit grain aggregation. With increasing content of $BiVO_4$ nanoparticles in $BiVO_4$/3DOM TiO_2, the nanoparticles of $BiVO_4$ grew from 30 nm to about 45.2 nm, indicating that the nanocrystals of $BiVO_4$ shifted to an agglomerated state as a result of densification, resulting in the growth of the crystal.

3.2 Morphology

Fig. 2 shows the SEM images of pure TiO_2 inverse opal (a and b), pure $BiVO_4$ nanoparticles (c and d) and the $BiVO_4$/3DOM TiO_2 nanocomposite (e and f) respectively.

The pure macroporous TiO_2 sample exhibits (Fig. 2a and b) a highly ordered three dimensional inverse opal structure with interconnected pores. The average pore size of the TiO_2 inverse opal is about 320 nm, being smaller than that of PS spheres used (350 nm) due to the contraction of the inverse opal structure after removing PS spheres upon calcination.

The pure $BiVO_4$ nanoparticles (Fig. 2c) exhibit dumbbell-like shapes, highlighting that the as-prepared $BiVO_4$ product is composed of countless dumbbell-like aggregates and nearly all of them adopt the same morphology. A single dumbbell aggregated from nanoparticles has a length ranging from 1 to 5 μm. Furthermore, we can notice that the surface of the obtained $BiVO_4$ sample is fairly rough as shown in Fig. 2c, which further indicates that every dumbbell is formed by an aggregation of

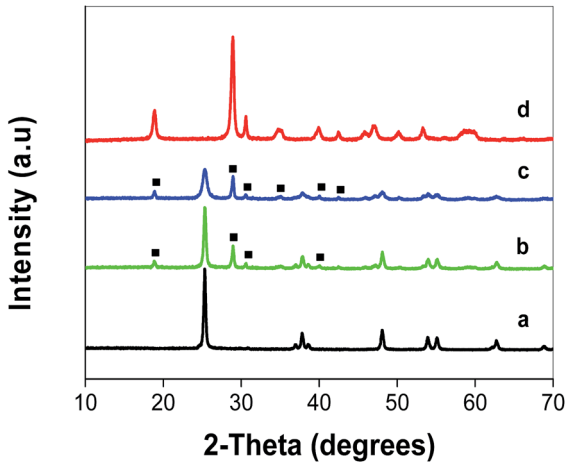

Fig. 1 X-ray diffraction patterns of (a) TiO_2 inverse opal, (b) 0.04$BiVO_4$/3DOM TiO_2, (c) 0.08$BiVO_4$/3DOM TiO_2 nanocomposites and (d) $BiVO_4$ nanoparticles.

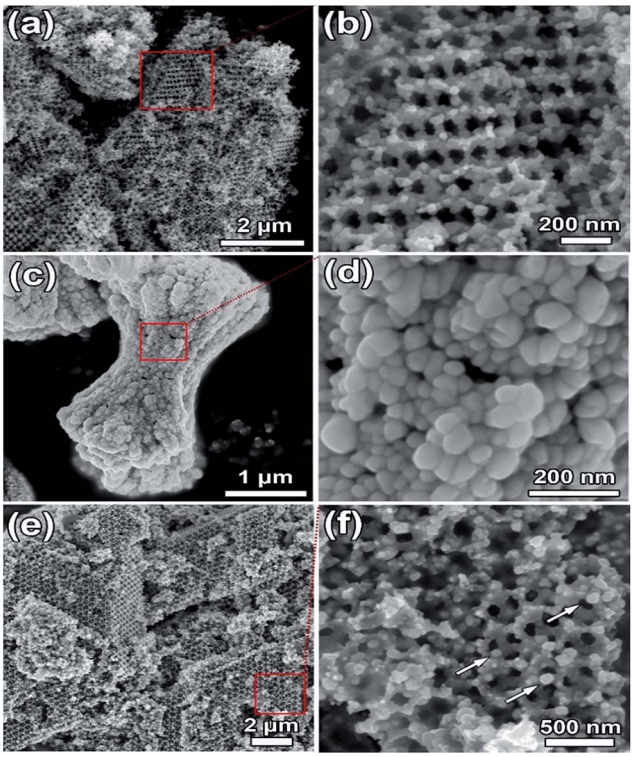

Fig. 2 SEM images of (a) and (b) inverse opal structural TiO_2 sample; (c) and (d) $BiVO_4$ sample; (e) and (f) inverse opal structural TiO_2 doping with the $BiVO_4$ sample ($BiVO_4$ particles are indicated by arrows).

nanoparticles. Fig. 2d presents an enlarged SEM image of the top structure of the dumbbell (Fig. 2c). It confirms that the $BiVO_4$ is an aggregate of small sphere-like nanoparticles of 30–60 nm. Thus the dumbbell-like $BiVO_4$ is assembled by the oriented aggregation of nanoparticles. This morphology is quite similar to that previously reported.[21]

The SEM micrograph in Fig. 2e confirms that a $BiVO_4$/3DOM TiO_2 nanojunction was obtained. The TiO_2 inverse opal support has a highly ordered structure with few defects. In this image it can be seen that the morphology of $BiVO_4$ has changed and the particle size has greatly increased to around 45 nm (as highlighted by the arrows in Fig. 2f). This is due to the effect of the calcination temperature. This observation is in very good agreement with the XRD results.

In order to get more information about the microstructure of the as-prepared products, further investigation was performed by TEM. The macrostructure of the pure TiO_2 inverse opal structure was examined by TEM, where the macropores can be clearly identified in Fig. 3a *via* a contrast in the image between voids and the material. As shown in Fig. 3b, TiO_2 is an aggregate of small nanoparticles. Fig. 3c shows a typical TEM image of dumbbell-like $BiVO_4$ nanoparticles. As can be seen in Fig. 3d, it confirms that $BiVO_4$ is an aggregate of small nanoparticles which is in good agreement with SEM observations. The TEM and STEM images and EDX mapping of the 0.08$BiVO_4$/3DOM TiO_2 nanocomposite are shown in Fig. 4. The 0.08$BiVO_4$/3DOM TiO_2 nanocomposite (Fig. 4a and b) has a dual morphology with small particles corresponding to $BiVO_4$ present on the 3DOM TiO_2 structure. The bismuth vanadate adopts a new morphology (Fig. 4b) with increased size after the formation of the nanocomposite (highlighted by arrows). The elemental compositions of the $BiVO_4$/3DOM TiO_2 heterojunctions were analyzed by energy dispersive X-ray spectroscopy (EDXS). As shown in Fig. 4c–e, the EDX mapping of 0.08$BiVO_4$/3DOM TiO_2 indicated

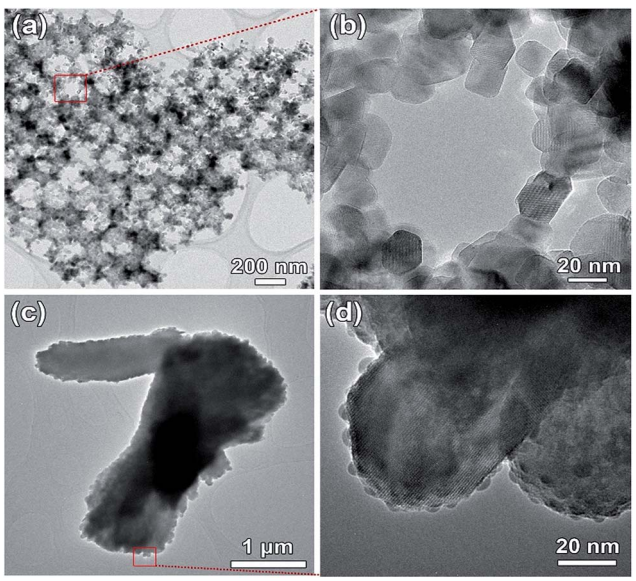

Fig. 3 TEM images of (a) and (b) inverse opal structural TiO_2 sample; (c) and (d) $BiVO_4$ nanoparticles.

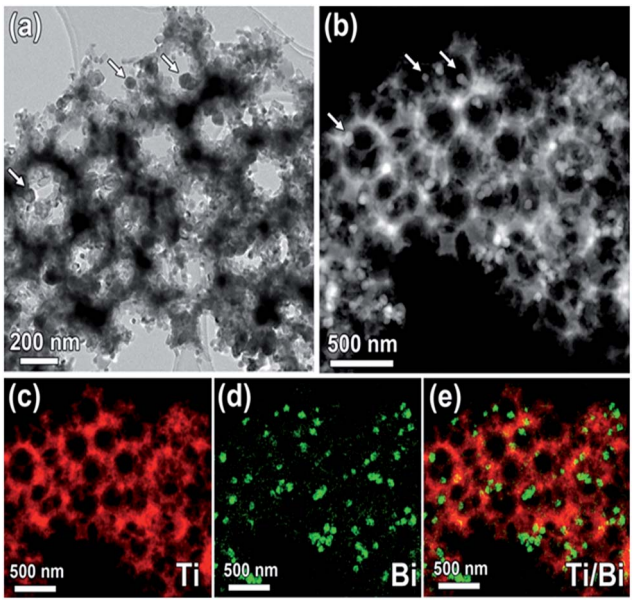

Fig. 4 (a) and (b) TEM and STEM images of the same zone of inverse opal structural TiO_2 doping with the $BiVO_4$ sample ($BiVO_4$ particles are indicated by arrows); (c–e) the corresponding EDX elemental mapping results.

the presence of Bi, V, Ti and O atoms in the sample. The red colour shows the Ti element and green represents bismuth vanadate nanoparticles which are homogeneously dispersed on the 3DOM TiO_2 IO structure. Fig. 4e shows the results for the combination of TiO_2 and $BiVO_4$. Fig. 4 evidences very clearly the intimate contact between the 3DOM TiO_2 IO structure and $BiVO_4$ nanoparticles.

3.3 Chemical states by X-ray photoelectron spectroscopy (XPS)

In order to elucidate the elemental composition, the oxidation states and the chemical environment of Bi, V and Ti elements in the $BiVO_4$/TiO_2 photocatalyst, XPS analysis was performed.

Fig. 5 shows the XPS spectra of the 0.08$BiVO_4$/3DOM TiO_2 nanocomposite (spectrum a), compared with the pure TiO_2 inverse opal structure (spectrum b) and pure $BiVO_4$ nanoparticles (spectrum c), in different spectral regions that correspond to different elements, revealing the binding energies for Bi 4f, Ti 2p, V 2p and O 1s of the as-prepared samples.

Fig. 5d–g show the high-resolution XPS spectra of the $BiVO_4$/TiO_2 sample. As shown in spectrum d, the binding energies of Bi $4f_{7/2}$ and Bi $4f_{5/2}$ are 159.0 and 164.3 eV, respectively, indicating that this element is present as Bi(III). The binding energy values are typical of bismuth in $BiVO_4$.[51] A shift of 0.3 eV to a higher binding energy in the peak positions of bismuth, as compared to pure $BiVO_4$ (158.7 eV and 164.0 eV), suggests that electron transfer from $BiVO_4$ to TiO_2 could occur, in accordance with the shift observed for bismuth. The high resolution V 2p spectrum reveals a doublet with peaks centred at 524 and 516.3 eV (spectrum e), which correspond to the V $2p_{1/2}$ orbit and V $2p_{3/2}$ orbit, respectively. These peaks also display binding energy

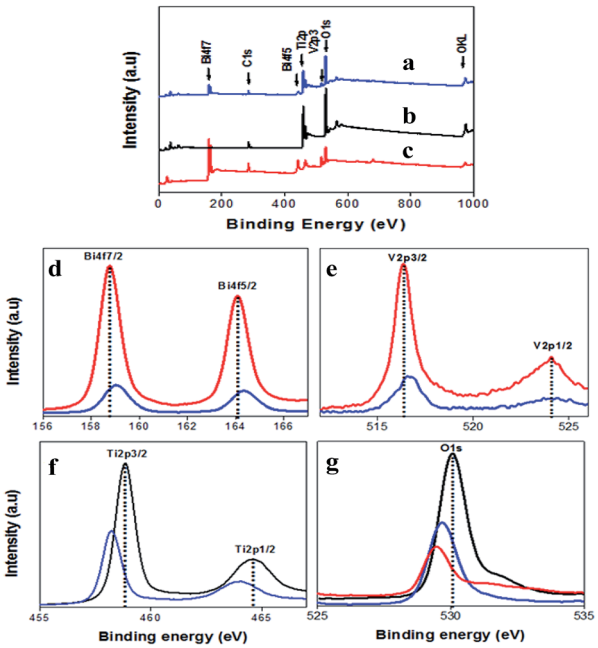

Fig. 5 Wide range XPS spectrum of the 0.08$BiVO_4$/3DOM TiO_2 nanocomposite (a), pure TiO_2 inverse opal (b) and pure $BiVO_4$ nanoparticles. High-resolution XPS spectra of Bi 4f (d), V 2p (e), Ti 2p (f) and O 1s (g) regions.

values typical of V(v) as reported in the literature.[51–54] Thus, the analysis of the V 2p core lines of the as-prepared sample clearly indicates the presence of V^{5+} oxidation states. Compared with pure $BiVO_4$, a slight shift of 0.3 eV is observed in the position peaks corresponding to V 2p (524.0 for the V $2p_{1/2}$ orbit and 516.3 eV for V $2p_{3/2}$).

Spectrum f depicts two bands with binding energies of 458.2 eV and 463.9 eV that are assigned to Ti $2p_{3/2}$ and Ti $2p_{1/2}$, respectively, corresponding to Ti^{4+} in a tetragonal structure such as anatase titania.[55] Compared to pure TiO_2, a shift of 0.6 eV to a lower binding energy in the peak positions of TiO_2 (458.8 eV and 464.5 eV) is observed, confirming the possible charge transfer between $BiVO_4$ and TiO_2. The high-resolution XPS spectrum of O 1s (spectrum g) shows a narrow peak at a binding energy of 529.6 eV. For pure $BiVO_4$ nanoparticles and the TiO_2 inverse opal structure, this peak was located at 529.4 and 530.0 eV, respectively. This asymmetric peak indicates that oxygen is present on the surface not only as lattice oxygen, but also as free oxygen.[51,53,54] All of these results gave the insight that the composite was formed by TiO_2 and $BiVO_4$. Moreover, the peaks for Bi 4f, V 2p, Ti 2p and O 1s in the $BiVO_4$/3DOM TiO_2 nanocomposite underwent a slight shift compared with those in pure $BiVO_4$ and TiO_2 resulting from the interaction between $BiVO_4$ and TiO_2 in the composite system.

3.4 Textural analysis

N_2 adsorption–desorption of the TiO_2 inverse opal, $BiVO_4$ and $BiVO_4$/3DOM TiO_2 nanocomposites revealed type II isotherms. For TiO_2 inverse opal, the pore size distribution plot calculated *via* the Barrett–Joyner–Halenda (BJH) method shows a narrow

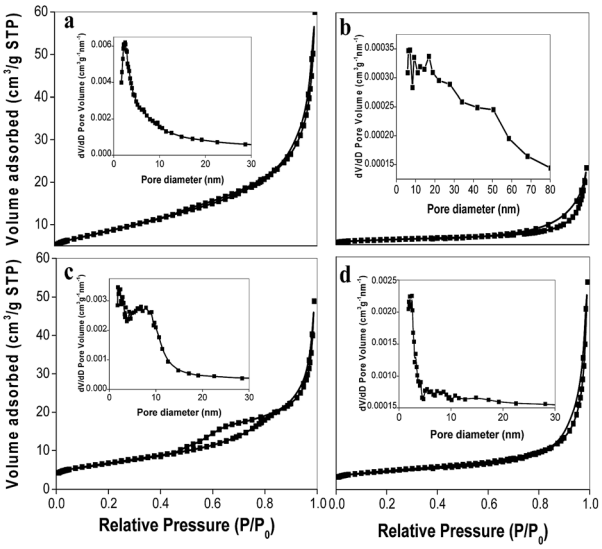

Fig. 6 N_2 adsorption–desorption isotherms and pore size distributions (insets) of the as-synthesized TiO_2 IO (a), $BiVO_4$ nanoparticles (b), 0.04$BiVO_4$/3DOM TiO_2 (c) and 0.08$BiVO_4$/3DOM TiO_2 (d) heterojunction photocatalysts.

Table 1 BET specific surface area, average pore diameter and pore volume of 3DOM TiO_2 and $BiVO_4$/3DOM TiO_2 heterojunction photocatalysts

Sample	S_{BET} m^2 g^{-1}	Pore size/nm	Pore volume cm^3 g^{-1}
$BiVO_4$	4	23	0.00032
TiO_2	30	2.3	0.0062
0.04$BiVO_4$/3DOM TiO_2	25	2.4	0.0028
0.08$BiVO_4$/3DOM TiO_2	17	2.5	0.0022

pore size distribution (inset Fig. 6a) centred at 2.3 nm, resulting from the aggregation of TiO_2 nanoparticles. The adsorbed nitrogen volume for TiO_2 inverse opal does not reach saturation at a high relative pressure p/p_o = 0.8–1.0, which indicates the presence of large macropores. Thus, the N_2 isotherm obtained for TiO_2 inverse opal reveals macroporosity which arises from the inverse opal structure. BET specific surface areas of pure $BiVO_4$ nanoparticles, pure TiO_2 inverse opal structure and $BiVO_4$/3DOM TiO_2 nanocomposites are shown in Table 1. $BiVO_4$ and TiO_2 inverse opal were found to have a surface area of 4 and 30 m^2 g^{-1}, respectively. For $BiVO_4$ nanoparticles (inset of Fig. 6b), the pore size distribution is quite large. The N_2 adsorption–desorption isotherms exhibit hysteresis arising from the aggregation of large particles. In the case of the two $BiVO_4$/3DOM TiO_2 nanocomposites (Fig. 6c and d), other than macroporosity from inverse opal structures, two pore sizes centred at 2.4 and 8 nm for 0.04$BiVO_4$/3DOM TiO_2 and 2.5 and 7 nm for 0.08$BiVO_4$/3DOM TiO_2 were observed, respectively. The pore size at 2.3–2.5 nm comes from the aggregation of TiO_2 nanoparticles whilst the pores of 7–9 nm come from the aggregation of $BiVO_4$ nanoparticles. When the amount of $BiVO_4$

nanoparticles is increased, the size of nanoparticles becomes bigger, larger pores can be formed, reducing the amount of pores of 7–9 nm. The XRD results confirmed the growth of nanoparticles with increasing $BiVO_4$ amount.

3.5 Optical properties

In order to understand the photocatalytic characteristics of the synthesized $BiVO_4/TiO_2$ nanocomposites, it is important to compare some of their typical properties such as reflectance and photoluminescence with those of pure $BiVO_4$ and TiO_2. The ordinary photographs and the UV-visible absorbance spectra of TiO_2 inverse opal, $BiVO_4$ nanoparticles and two $BiVO_4/TiO_2$ nanocomposites are shown in Fig. 7A and B, respectively. From Fig. 7A it can be seen that titania inverse opal (a) has a white color. On adding bismuth vanadate (d), which has a strong yellow color, the tone of the white color changes in two different manners. In the sample with 0.04$BiVO_4$/3DOM TiO_2 (b), the color turns to a light yellow tone. On increasing the amount of $BiVO_4$ to 0.08 (c), the yellow colour becomes more intense. It can be clearly seen that with an increasing amount of $BiVO_4$, the absorption edge of the $BiVO_4$/3DOM TiO_2 nanocomposite is red shifted to longer wavelengths within the visible-light range (spectra b and c of Fig. 6B), with the spectral response range of TiO_2 being extended. The $BiVO_4$ nanoparticle sample (spectrum d of Fig. 7B) showed an absorption edge around 527 nm, which could be responsible for any potential visible-light induced photocatalytic activity.

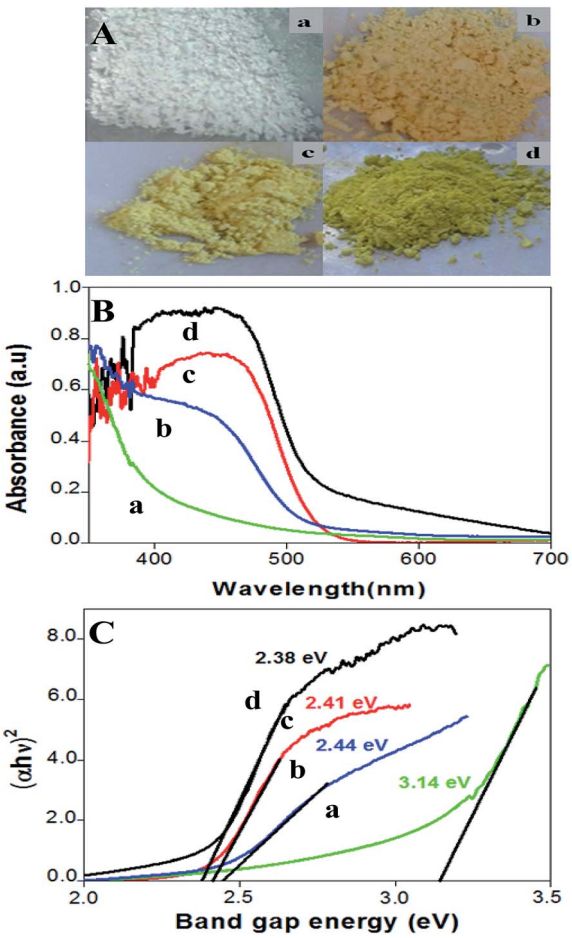

Fig. 7 (A) Ordinary photographs, (B) UV-vis diffuse absorbance spectra, and (C) a plot of $(\alpha h\nu)^{1/2}$ *versus* bandgap energy of (a) 3DOM TiO_2, (b) 0.04$BiVO_4$/3DOM TiO_2, (c) 0.08$BiVO_4$/3DOM TiO_2 and (d) $BiVO_4$ photocatalysts.

The steep absorption edge in the visible range indicates that the absorption of visible light is not due to the transition from impurity levels but due to the bandgap transition,[35,36] originating from the charge transfer response of monoclinic $BiVO_4$ from the valence band populated by the hybridization of the O 2p orbital and Bi 6s orbital to the conduction band formed by the V 3d orbital.[42] As can be seen, the absorbance of the $BiVO_4$/3DOM TiO_2 nanocomposites in the visible light region increases with increasing the amount of bismuth vanadate (spectra b–d of Fig. 6B). The change in light absorption can be inferred even from the colours of the various compounds.

The bandgap energies of the as-prepared samples could thus be estimated from a plot of $(\alpha h\nu)^{1/2}$ *versus* photon energy $(h\nu)$ *via* the Kubelka–Munk method:[56–58] $\alpha h\nu = A(h\nu - E_g)^{1/2}$, where α, h, ν, E_g, and A are the absorption coefficient, Planck's constant, light frequency, bandgap energy, and a constant, respectively.

The intercept of the tangents to the x-axis gives a good approximation of the bandgap energy for the materials. As shown in Fig. 7C, the estimated bandgaps of the $BiVO_4$ nanoparticles, TiO_2 inverse opal, 0.04$BiVO_4$/3DOM TiO_2 and 0.08$BiVO_4$/3DOM TiO_2 photocatalysts were about 2.37, 3.15, 2.45 and 2.4 eV, respectively. From these results it can be confirmed that the $BiVO_4$ semiconductor acts as a visible light absorber for TiO_2, leading to effective separation of photoinduced electron–hole pairs, thus reducing the likelihood of recombination. In order to investigate whether this could be possible, photoluminescence (PL) measurements were carried out.

Fig. 8 shows the photoluminescence (PL) emission spectra of pure $BiVO_4$ nanoparticles, pure TiO_2 inverse opal and $BiVO_4$/3DOM TiO_2 nanoheterostructured photocatalysts, which have been used to provide information on the efficiency of charge carrier trapping, migration and transfer.

It is very helpful to understand the fate of the electron–hole pairs in semiconductors as PL emission stems from the recombination of free carriers. The PL intensity depends on the recombination of excited electrons and holes. The lower the PL emission intensity is, the lower is the recombination property of the sample. As can be seen, $BiVO_4$ (spectrum a) exhibits a weak emission at 525 nm which is caused by electron–hole recombination at surface traps. The overall PL emission intensity of $BiVO_4$ is the lowest, indicating the very low recombination rate of electron–hole pairs in this material. It can also be observed that the bare TiO_2 (spectrum d) exhibits a strong PL signal in the range of 400 to 450 nm, and has four obvious PL peaks at about 442, 460, 493 and 525 nm, respectively, possibly the former mainly resulting from band edge free excitons and the latter mainly from binding excitons.[59,60] The overall PL emission intensity of TiO_2 is the highest, showing its highest recombination rate of electron–hole pairs, being unfavourable for photocatalysis. However, the characteristic emission of TiO_2 is

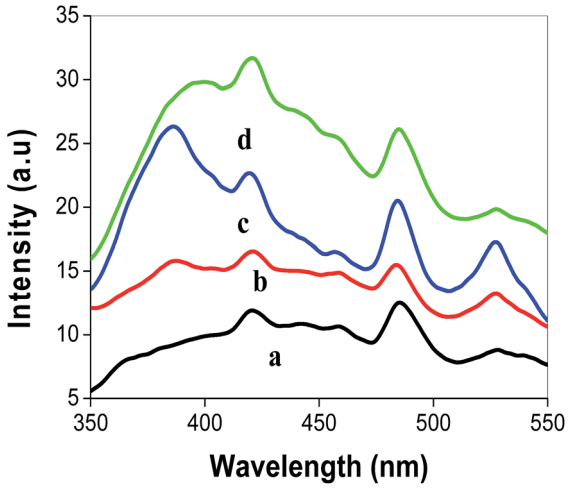

Fig. 8 Photoluminescence spectra of (a) pure $BiVO_4$, (b) $0.08BiVO_4/TiO_2$, (c) $0.04BiVO_4/TiO_2$ and (d) pure TiO_2.

significantly affected after the introduction of $BiVO_4$ nanoparticles and the intensity is progressively reduced with increasing $BiVO_4$ amount in the 3DOM TiO_2 IO structure. This behaviour shows that efficient charge or energy transfer occurs at the $BiVO_4/TiO_2$ heterojunction interface. The observation of PL bands depends on the excitation wavelengths. For example, no PL bands when the excitation wavelength is 320 nm for $BiVO_4$ nanoparticles while some PL bands, in spite of low intensity, are indeed observed with an excitation wavelength of 515 nm (Fig. 2S†). These are due to different electron–hole generation and recombination rates between different bands (Fig. 3S†).

The positions of the CB and VB of TiO_2 and those of the $BiVO_4$ and XPS results also suggest that interactions between $BiVO_4$ and TiO_2 involve charge transfer of photoexcited electrons from the conductive band of the donor $BiVO_4$ to the empty electronic states of the acceptor TiO_2 and a better charge separation in space in $BiVO_4$/3DOM TiO_2 nanocomposites. These observations are in good agreement with those observed by the XPS study. More details will be given in the following sections.

3.6 Photocatalytic activity

The degradation of rhodamine B (RhB) under visible light irradiation was conducted, as a test reaction, in the presence of each material. The absorption spectrum in the range of 500–600 nm for different time intervals for the $0.08BiVO_4$/3DOM TiO_2 nanocomposite photocatalyst is shown in Fig. 9A as an example. It has been shown that the major absorption peaks of RhB, located at around 554 nm, diminished gradually under visible light irradiation in the presence of the $BiVO_4$/3DOM TiO_2 nanocomposite. The photocatalytic efficiencies (C/C_0) of pure $BiVO_4$ nanoparticles, pure 3DOM TiO_2 inverse opal, two reference samples (phy-mix $0.08BiVO_4$/3DOM TiO_2 IO and $0.08BiVO_4$/P25-TiO_2 nanoparticles) and two $BiVO_4/TiO_2$ nanocomposites are illustrated in Fig. 9B. The blank experiment of

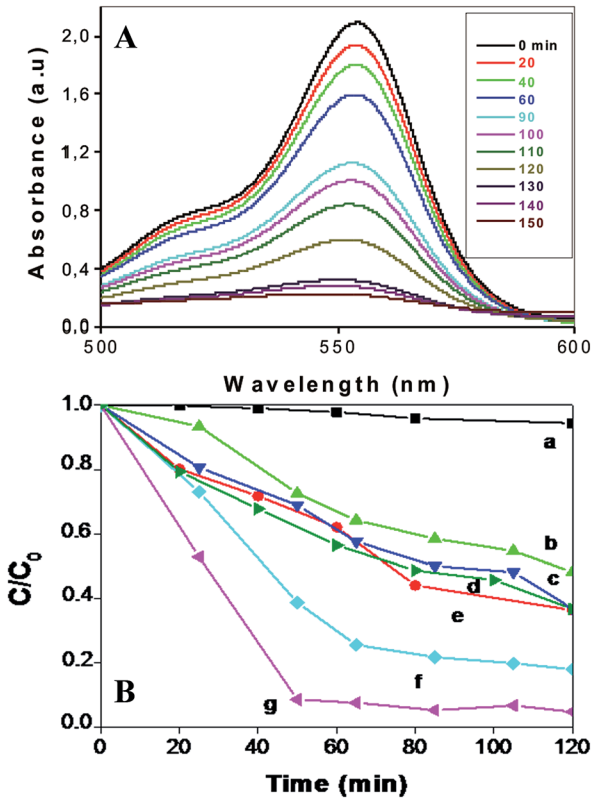

Fig. 9 (A) The temporal evolution of the absorption spectra of the RhB solution in the presence of the $0.08BiVO_4$/3DOM TiO_2 photocatalyst under visible-light illumination. (B) The variation of RhB concentrations (C/C_0) with irradiation time over different photocatalysts: (a) a blank, (b) $BiVO_4$ nanoparticles, (c) pure 3DOM TiO_2, (d) phy-mix $0.08BiVO_4$/3DOM TiO_2, (e) $0.08BiVO_4$/P25 TiO_2, (f) $0.04BiVO_4$/3DOM TiO_2 and (g) $0.08BiVO_4$/3DOM TiO_2.

RhB degradation without the presence of a photocatalyst is shown in curve (a) of Fig. 9B. A very low degradation rate of RhB, similar to that reported in the literature, was observed and can be neglected. It can clearly be observed that for all samples the degradation of RhB increases gradually with increasing irradiation time. $BiVO_4$ nanoparticles exhibit very poor photocatalytic activity, with only 22% of RhB being degraded in 50 min, despite its strong absorption in the visible region. Under the same illumination conditions 28% of the RhB solution was degraded by 3DOM anatase TiO_2 inverse opal. However due to its wide bandgap energy in the UV range, TiO_2 could not absorb in the visible range. Thus theoretically, no possible degradation of dye molecules by TiO_2 can be expected. Nevertheless, good degradation rate can be expected for the 3DOM IO structure. We will explain this observation in the following paragraph. The photocatalytic performance of TiO_2 can be improved by coupling catalysts with sensitizers leading to the $BiVO_4/TiO_2$ nanocomposite proposed herein with a narrow bandgap and thus higher photocatalytic activity. The increase in performance was demonstrated by a superior photodegradation of RhB, with the destruction of 80% and 95% RhB over a 120 min period in the presence of $0.04BiVO_4$/3DOM TiO_2 and $0.08BiVO_4$/3DOM TiO_2, respectively.

It has been reported that the photocatalytic degradation process of RhB follows first-order kinetics.[60] The kinetics of RhB degradation with the different samples is illustrated in Fig. 10. The rate constants for the pure $BiVO_4$ nanoparticles, pure TiO_2 inverse opal, phy-mix 0.08$BiVO_4$/3DOM TiO_2, 0.08$BiVO_4$/P25-TiO_2, 0.04$BiVO_4$/3DOM TiO_2 and 0.08$BiVO_4$/3DOM TiO_2 photocatalysts are calculated to be 0.0062, 0.0078, 0.0079, 0.0084, 0.0152 and 0.0256 min^{-1} respectively. From the rate constants (k) in Fig. 10, it can be inferred that the order for the photodegradation rates is: 0.08$BiVO_4$/3DOM TiO_2 > 0.04$BiVO_4$/3DOM TiO_2 > 0.08$BiVO_4$/P25-TiO_2 > phy-mix 0.08$BiVO_4$/3DOM TiO_2 ≥ 3DOM TiO_2 > $BiVO_4$. The nanocomposite of 0.08$BiVO_4$/3DOM TiO_2 has photocatalytic activity 4 times and 3 times higher than pure $BiVO_4$ and 3DOM TiO_2, respectively, showing the high impact of the $BiVO_4$/3DOM TiO_2 heterojunction on the photocatalytic performance. The reference sample prepared by the physical mixing of $BiVO_4$ and 3DOM TiO_2 IO has similar photocatalytic activity to that of pure 3DOM TiO_2 IO, indicating that the introduction of a low amount of $BiVO_4$ into 3DOM TiO_2 IO by physical mixing does not induce an effect on the photocatalytic activity and hence the importance of the intimate contact between $BiVO_4$ and the 3DOM TiO_2 IO structure. Another reference sample 0.08$BiVO_4$/P25-TiO_2 prepared by the same hydrothermal method as $BiVO_4$/3DOM TiO_2 showed higher photocatalytic activity than pure 3DOM TiO_2, the physical mixing sample and pure $BiVO_4$ nanoparticles, but it was much lower than that of $BiVO_4$/3DOM TiO_2 nanocomposites, confirming again the enhancement of photocatalytic activity by the intimate contact between $BiVO_4$ and TiO_2 and the importance of the 3DOM inverse opal structure.

It is clear that the photocatalytic activity of $BiVO_4$/TiO_2 nanocomposite photocatalysts is strongly dependent on the amount of $BiVO_4$. The photodegradation activity of (x) $BiVO_4$: TiO_2 increases remarkably with an increasing amount of $BiVO_4$ up to $x = 0.08$. The enhanced photocatalytic activity may originate from the interfacial transfer of electrons and holes as observed by PL and XPS studies. The lifetime of the charge carriers is increased and thus the recombination of electron–hole pairs can be inhibited, which resulted in an elevation of the photocatalytic efficiency of TiO_2 under visible-light irradiation. As a comparison, Cao *et al.*[24] studied the photocatalytic activity of the $BiVO_4$/TiO_2 composite under simulated sun-light irradiation. The photocatalytic activities of the $BiVO_4$/TiO_2 composites with different ratios were evaluated by the degradation of RhB at room temperature. They found that 20 wt% TiO_2/$BiVO_4$ shows higher activity with a constant rate equal to 0.04 min^{-1}.

3.7 Photocatalysis mechanism

The coupling of different semiconductor oxides seems to be useful in order to absorb a wide range of solar radiation and to achieve more efficient electron–hole pair separation when under irradiation and, consequently, higher photocatalytic activity. A schematic representation of our $BiVO_4$/3DOM TiO_2 nanocomposites with bismuth vanadate nanoparticles incorporated in the 3DOM inverse opal TiO_2 matrix is presented in Fig. 11A. The combination of $BiVO_4$ and TiO_2 has attracted much attention recently in photocatalysis.[20,24–31] However, the photocatalysis promoting mechanism remains unclear and diverging. Hu *et al.*[26] proposed a band configuration where the CB and VB of $BiVO_4$ were positioned at locations higher than the CB and VB of pure TiO_2, respectively. Under visible light irradiation, the electrons of the VB of $BiVO_4$ are promoted to its CB, leaving holes behind. Electrons in the CB of $BiVO_4$ can now be transferred to the CB of TiO_2. Electrons in the CB of TiO_2 are

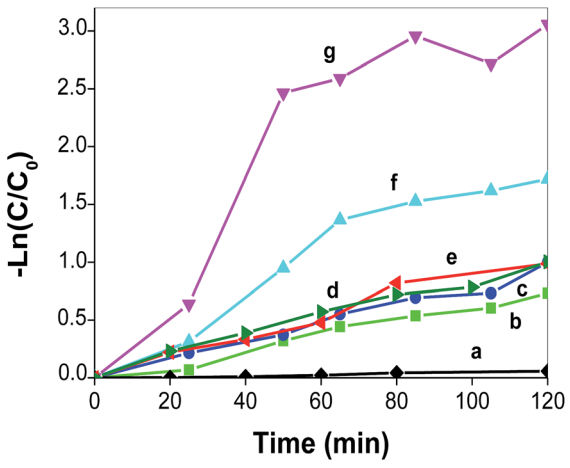

Fig. 10 Kinetics of RhB degradation with (a) a blank, (b) $BiVO_4$ nanoparticles, (c) 3DOM TiO_2, (d) physical mixture of 0.08$BiVO_4$/3DOM TiO_2, (e) 0.08$BiVO_4$/P25-TiO_2 nanoparticles, (f) 0.04$BiVO_4$/3DOM TiO_2 and (g) 0.08$BiVO_4$/3DOM TiO_2 nanocomposite photocatalysts.

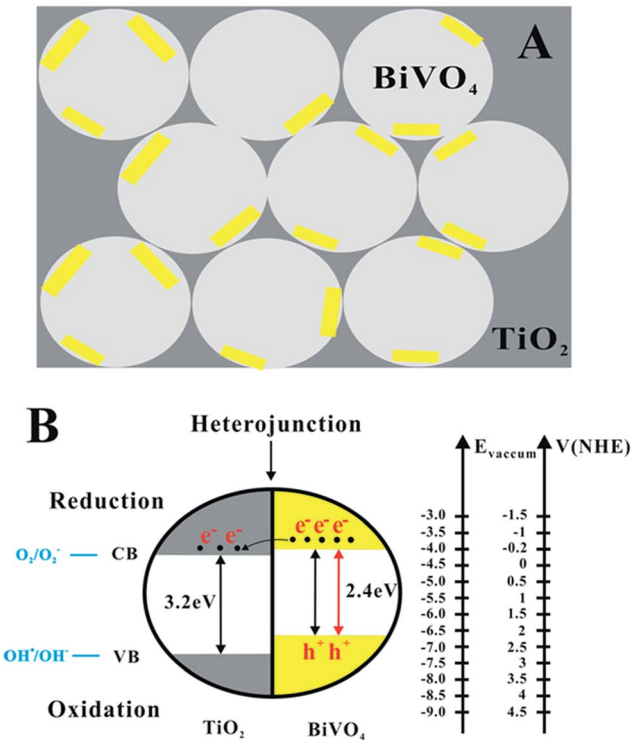

Fig. 11 (A) Schematic representation of $BiVO_4$/TiO_2 nanocomposites. (B) Energy band diagram and charge transfer processes in $BiVO_4$/TiO_2 nanostructured photocatalysts under visible light irradiation.

good reductants which can capture the adsorbed O_2 and reduce it to $O_2^{\bullet-}$ to oxidize dye molecules. The holes at the VB of $BiVO_4$ can react with OH^- to give rise to $OH^\bullet$ which can also be used for the degradation of dye molecules. The authors claimed that $BiVO_4$ played the role of a light sensitizer. The photodegradation of organic molecules occurred at the surface of $BiVO_4$. However, our present results show that pure $BiVO_4$ gave very low photocatalytic activity. A different electronic mechanism should thus be involved. Zhang *et al.*[25] proposed one such different electronic mechanism. On the basis of their calculations, they placed the CB and VB of $BiVO_4$ between the CB and VB of TiO_2. They suggested that under both UV and visible light irradiation the photogenerated electrons from RhB dye molecules are transferred to the CB of TiO_2 which are in turn transferred to the CB of $BiVO_4$, leaving the holes in the VB of TiO_2. They proposed that the reduction of RhB occurs in the CB of $BiVO_4$ and the oxidation of RhB can take place in the VB of both TiO_2 and $BiVO_4$. Colon *et al.*[31] postulated a similar electronic mechanism with similar positions of the CB and VB of TiO_2 and those of $BiVO_4$. However, this proposition concerning the positions of the CB and VB of TiO_2 and those of $BiVO_4$ remains to be confirmed. In some very recent papers, the positions of the CB and VB of TiO_2 and $BiVO_4$ were revisited. A generally accepted point is that under visible light irradiation, electrons of the VB of $BiVO_4$ will be firstly excited to the CB of $BiVO_4$, leaving holes behind and these photogenerated electrons will be transferred to the CB of TiO_2. Tang *et al.*[30] pointed out that electron transfer from $BiVO_4$ to TiO_2 is feasible since E_{CB} of TiO_2 is considered to be located just under the conduction band of $BiVO_4$. Fu *et al.*[29] in their excellent recent paper confirmed this suggestion that electrons are transferred from $BiVO_4$ to TiO_2. $BiVO_4$ can be considered as a light sensitizer for TiO_2.

On the basis of the above analysis, our XPS results, photocatalytic performance of a series of materials studied herein and the fact that pure $BiVO_4$ gives an unexpectedly low photocatalytic activity in the degradation of RhB dye molecules, a new energy band diagram of the $BiVO_4/TiO_2$ heterojunction photocatalysts is proposed and presented in Fig. 11B. It should be taken into account that the work function for RhB is −5.45 eV and −3.08 eV for excited RhB.[61] For $BiVO_4$, a valence band (VB) edge potential of 1.90 V (NHE scale) was reported by Su *et al.*[62] while the VB of TiO_2 was reported to be 2.82 V (NHE scale) by Hagfeldt *et al.*[63] and Sayama *et al.*[64] The measured bandgap energies of TiO_2 and $BiVO_4$ by the present study were around 3.15 and 2.37 eV, respectively. The position of a conduction band (CB) edge is determined by $E_{CB} = E_{VB} - E_g$. Thus, the calculated CB energies of $BiVO_4$ and TiO_2 were −0.47 and −0.27 eV, respectively. The difference in the conduction band energies between $BiVO_4$ and TiO_2 allows the transfer of electrons from the conduction band of $BiVO_4$ to that of TiO_2 since the position of the CB of TiO_2 is just under that of $BiVO_4$.

When the system is irradiated with visible light, $BiVO_4$ is activated to generate electron–hole pairs. An electron (e^-) is promoted from the valence band, VB, into the conduction band, CB, of $BiVO_4$, leaving a hole (h^+) behind. The excited-state electrons produced by $BiVO_4$ can be injected into the conduction band of the coupled TiO_2 due to the intimate matching of the electric fields between the two materials and because the position of the CB of TiO_2 is just under the CB of $BiVO_4$ as indicated by Tang *et al.*[30] The electron transfer is now feasible. The electron and holes are physically separated in space, reducing the opportunity of their recombination. The conduction electrons at the TiO_2 side are good reductants which can be scavenged by molecular oxygen, O_2, to yield the superoxide radical anion O_2^-. The holes at the VB of $BiVO_4$ will interact with hydroxyl groups to form $OH^\bullet$ radicals. It is well known that the $OH^\bullet$ radical is a powerful oxidizing agent capable of degrading most pollutants. In the present case, RhB dye model molecules will be degraded by O_2^- and $OH^\bullet$ radicals. Anatase TiO_2 inverse opal has a very large gap so that no electrons can be promoted from the VB to CB, thus no electron–hole pairs can be formed under visible light irradiation.

Concerning pure $BiVO_4$ nanoparticles, the bandgap is around 2.4 eV and located in the visible light zone. However, an unexpected low photocatalytic activity towards RhB dye molecules, even lower than that of the anatase TiO_2 inverse opal structure, has been observed. The same phenomenon that the photocatalytic activity of monoclinic $BiVO_4$ in the degradation of phenol is lower than that of pure anatase TiO_2 in the visible light range has been previously reported by Colon *et al.*[20] The low photocatalytic activity of the single phase of $BiVO_4$ photocatalysts was also pointed out by Fresno *et al.*,[27] Li *et al.*[21] and Jiang *et al.*[33] The lower photocatalytic activity of pure monoclinic $BiVO_4$ compared to 3DOM TiO_2 observed in the present study can be due to two different reasons. Firstly, although our PL study showed that pure monoclinic $BiVO_4$ has a very low recombination rate of electrons–holes, due to its intrinsic characteristics such as the very poor adsorptive performance towards organic dye molecules and the inefficient migration of photogenerated electron–hole pairs to the surface for photocatalytic reactions, the pure monoclinic $BiVO_4$ presented an unexpectedly low photocatalytic activity in the visible light degradation of organic dye pollutants.[21,33] The combination with TiO_2 can largely improve the adsorption properties and migration rate of electron–hole pairs towards the surface of $BiVO_4$/3DOM TiO_2 facilitating electron transfer from the CB of $BiVO_4$ to the CB of TiO_2. Secondly, as RhB molecules can absorb visible light, it is possible that some electrons can be promoted from the HOMO (−5.45 eV) to LUMO (−3.08 eV) and these electrons of RhB can migrate to the CB of anatase TiO_2 to generate reactive O_2^- to degrade RhB dye molecules. This is why the degradation of RhB can be observed on anatase TiO_2 inverse opal in the visible light range although TiO_2 absorbs only UV light and the activity is even higher than that of $BiVO_4$ nanoparticles.

It is worth noting that our 3DOM TiO_2 presented very interesting photodegradation activity in the visible zone. It is well-known that TiO_2 has a large electronic bandgap and cannot absorb visible light and should not exhibit photodegradation activity of dye molecules in the visible zone. The dye molecule degradation rate of pure TiO_2 inverse opal has been reported by Lee *et al.*[65] Their TiO_2 IO sample gave a degradation rate of 5% after 120 minutes, much lower than the photocatalytic activity observed for our pure TiO_2 inverse opal. The difference is

because of the following reasons. (1) Different preparation conditions: their TiO_2 IO sample was calcined at 850 °C and contained mainly the rutile phase, while our sample was calcined at 550 °C and contained only the anatase phase. It is well known that the rutile phase is less active than the anatase phase. (2) Different photocatalytic conditions: in their case they used methylene blue while in our case we used RhB as the reactant. (3) Different characteristics of samples: their sample had a macropore size of 500 nm while our sample had a macropore size of 250 nm. Their sample was in the shape of a film while our sample was in a powder form. Our sample had a higher surface area, *i.e.* higher contact area. Due to the above reasons, their sample presented different activity compared to our 3DOM TiO_2 powder. However, one point is important to underline that our bare 3DOM TiO_2 IO sample gave an unexpectedly high degradation rate of 28%. The reason is quite probably related to the 3DOM TiO_2 IO structure which could generate the slow photon effect so that the photocatalytic activity was enhanced. Ozin's group and our group have reported this effect for TiO_2 IO in the form of films for visible light and UV light in gas phase[47–49] and liquid phase[39,49,50] photocatalytic degradation of dye molecules, respectively. Our present sample could have exhibited this slow photon effect that facilitated enhancement in photocatalytic activity even in the visible light zone, in good agreement with the observation made by Ozin *et al.* with a similar pore size of TiO_2 IO.[47–49] That is why we observed a degradation activity of 28% which is not observed for P25 in the visible light zone. We are working on this effect to better investigate the slow photon effect in the visible light zone to enhance the photocatalytic activity. However, due to the powder form of the sample, the investigation is much more difficult than that of film shaped samples. Another point is that the 3DOM TiO_2 can provide a more active surface area, more contact area and increased mass transfer because of its highly accessible 3D porosity. We prepared a reference sample by the deposition of $BiVO_4$ nanoparticles on P25-TiO_2 nanoparticles using the same hydrothermal preparation method. The photocatalytic activity of 3DOM $BiVO_4/TiO_2$ nanocomposites is much higher than that of the $BiVO_4/TiO_2$-P25 nanocomposite, showing very clearly the effect of the 3DOM TiO_2 inverse opal structure.

We also performed a control experiment for the photodegradation of RhB using a physical mixture (*e.g.*, grinding) of $BiVO_4$ dumbbell nanoparticles and 3DOM TiO_2 powder and compared its photocatalytic activity with that of the $BiVO_4$/3DOM TiO_2 nanocomposite. It is evidenced that the photocatalytic activity of the physical mixture (*e.g.*, grinding) of $BiVO_4$ dumbbell and 3DOM TiO_2 is very similar to that of the pure 3DOM TiO_2 inverse opal structure and slightly higher than that of pure $BiVO_4$ dumbbell, but much lower than that of $BiVO_4$/3DOM TiO_2 IO nanocomposites prepared by careful deposition of $BiVO_4$ nanoparticles on the 3DOM TiO_2 IO structure to have an intimate contact between the two phases, illustrating the advantage of the intimate contact between $BiVO_4$ nanoparticles and the 3DOM inverse opal structure.

When the narrow bandgap sensitizer $BiVO_4$ and the large bandgap photocatalyst TiO_2 are in intimate contact in 3DOM $BiVO_4/TiO_2$ nanocomposites, drawbacks such as the rapid e^-–h^+ recombination that occurs in TiO_2, the poor adsorption properties and low migration rate of electrons–holes of pure $BiVO_4$ towards its surface and the absence of excitation of TiO_2 in the visible light range can all be avoided. Under visible light irradiation, the electrons in the CB excited from the VB of $BiVO_4$ can migrate to the CB of the TiO_2 photocatalyst to generate very reactive O_2^- species. The h^+ generated in the VB of $BiVO_4$ can react with hydroxyl groups to form the oxidizing agent OH^-. Both O_2^- and OH^- at the surface of the $BiVO_4$/3DOM TiO_2 nanocomposite will degrade RhB dye pollutants adsorbed by TiO_2. $BiVO_4$ in our $BiVO_4$/3DOM TiO_2 nanocomposites plays the role of a light sensitizer, accelerating the photodegradation rate of RhB by 3DOM TiO_2. Larger the amount of $BiVO_4$, greater is the sensitizing effect, *i.e.* better light absorption (suggested by diffuse reflectance) and better charge separation effect (suggested by PL). These two effects make the 0.08$BiVO_4$/3DOM TiO_2 sample a better photocatalyst. However, there exists an optimal amount of $BiVO_4$. We are working to determine this optimal amount. Larger the amount of $BiVO_4$ in TiO_2 inverse opal, greater the number of electrons–holes generated in the $BiVO_4$/3DOM TiO_2 nanocomposite, and higher is the photocatalytic activity. It is clear that the 3DOM $BiVO_4/TiO_2$ nanocomposite with intimate contact can provide an efficient way to design long-lived visible light excited charge carriers for photocatalysis.

4. Conclusions

Novel 3DOM $BiVO_4/TiO_2$ nanocomposites have been successfully synthesized. According to the UV-vis DRS results, the absorption of $BiVO_4/TiO_2$ nanocomposites increased in the visible region. Moreover, the low bandgap energy of $BiVO_4/TiO_2$ nanocomposites also influenced dye degradation and showed significant promise for these nanocomposites to be employed as effective visible light photocatalysts for dye wastewater treatment, photocatalytic water splitting, CO_2 reduction and other solar applications. In fact, by coupling different bandgap semiconductors such as TiO_2 and $BiVO_4$, the resultant nanocomposites facilitate the separation of the photogenerated carriers under the internal field induced by the different electronic band structures of the semiconductors. Thus the photocatalytic activity of TiO_2 inverse opals was efficiently improved. It can be concluded that adding narrow bandgap energy materials as light sensitizers to TiO_2 is a very promising method to render 3DOM TiO_2 inverse opals more efficient in the photodegradation of organic pollutants and in the water splitting reaction under visible light. Thus, compared to 3DOM TiO_2 the 3DOM $BiVO_4/TiO_2$ nanocomposites presented herein exhibit higher photocatalytic activities and can be considered as more efficient as they promote visible-light-driven photocatalysis. Increasing the $BiVO_4$ amount in nanocomposites can increase the photogenerated charge separation time and in consequence improve the photocatalytic performance again. In the present work, the benefits of 3D porosity and high surface area of the TiO_2 inverse opal structure were essential for the accessibility of dye molecules to photocatalysts and for better dispersion of $BiVO_4$ nanoparticles. However, the benefit of the slow photon

effect of the 3DOM TiO_2 inverse opal photonic crystal structure has not been studied. The future work will focus on the optimisation of the amount of $BiVO_4$ in nanocomposites, the study of other large bandgap photocatalysts such as ZnO and taking equal attention to the possible slow photon effect of the 3DOM TiO_2 inverse opal.

Acknowledgements

This work was realized with the financial support of the Belgian FNRS (Fonds National de la Recherche Scientifique). This research used resources of the Electron Microscopy Service located at the University of Namur. This Service is a member of the "Plateforme Technologique Morphologie – Imagerie". The XPS analyses were made in the LISE, Department of Physics of the University of Namur thanks to Dr P. Louette. This work was also supported by Changjiang Scholars and the Innovative Research Team (IRT1169) of the Ministry of Education of the People's Republic of China. B. L. Su acknowledges the Chinese Central Government for an "Expert of the State" position in the Program of the "Thousand Talents" and a Clare Hall Life Membership at the Clare Hall and the financial support of the Department of Chemistry, University of Cambridge. G. Van Tendeloo and Z. Y. Hu acknowledge support from the EC Framework 7 program ESTEEM2 (Reference 312483).

Notes and references

1 S. J. Liao, D. G. Huang, D. H. Yu, Y. L. Su and G. Q. Yuan, *J. Photochem. Photobiol., A*, 2004, **168**, 7–13.
2 H. Li, G. Liua and X. Duana, *Mater. Chem. Phys.*, 2009, **115**, 9–13.
3 W. S. Lu, G. C. Xiao, D. Z. Li, X. Z. Fu and X. X. Wang, *Chin. J. Inorg. Chem.*, 2005, **21**, 1495–1499.
4 H. Irie, Y. Watanabe and K. Hashimoto, *J. Phys. Chem. B*, 2003, **107**, 5483–5486.
5 O. Diwald, T. L. Thompson and T. Zubkov, *J. Phys. Chem. B*, 2004, **108**, 6004–6008.
6 N. Serpone, P. Maruthamuthu, P. Pichat, E. Pelizzetti and H. Hidaka, *J. Photochem. Photobiol., A*, 1995, **85**, 247–255.
7 L. M. Peter, D. Jason Riley, E. J. Tull and K. G. UpulWijayantha, *Chem. Commun.*, 2002, **10**, 1030–1031.
8 W. Liu, S. F. Chen, S. J. Zhang, W. Zhao, H. Y. Zhang and X. L. Yu, *J. Nanopart. Res.*, 2010, **12**, 1355–1366.
9 I. Bedjat and P. Kamat, *J. Phys. Chem.*, 1995, **99**, 9182–9188.
10 J. Engweiler, J. Harf and A. Baiker, *J. Catal.*, 1996, **159**, 259–269.
11 J. Xu, W. Z. Wang, S. Sun and L. Wang, *Appl. Catal., B*, 2012, **111–112**, 126–132.
12 Y. Liu, F. Xin, F. Wang, S. Luo and X. Yin, *J. Alloys Compd.*, 2010, **498**, 179–184.
13 E. V. Skorb, E. A. Ustinovich, A. I. Kulak and D. V. Sviridov, *J. Photochem. Photobiol., A*, 2008, **193**, 97–102.
14 L. Huang, F. Peng, H. J. Wang, H. Yu and Z. Li, *Catal. Commun.*, 2009, **10**, 1839–1843.
15 Z. D. Meng, L. Zhu, J. G. Choi, C. Y. Park and W. C. Oh, *Nanoscale Res. Lett.*, 2011, **6**, 459–469.
16 D. N. Ke, H. J. Liu, T. Y. Peng, X. Liu and K. Dai, *Mater. Lett.*, 2008, **62**, 447–450.
17 K. Vinodgopal and P. V. Kamat, *Environ. Sci. Technol.*, 1995, **29**, 841–845.
18 Y. Bessekhouad, D. Robert and V. Weber, *Catal. Today*, 2005, **101**, 315–321.
19 A. Zhang and J. Zhang, *Mater. Lett.*, 2009, **63**, 1939–1942.
20 S. Obregon, S. W. Lee and G. Colon, *Dalton Trans.*, 2014, **43**, 311–316.
21 Y. K. Li, J. Y. Dong, Y. F. Wang, J. Y. Sun, Y. F. Li and Y. Q. Pi, *J. Mol. Catal. A: Chem.*, 2014, **387**, 138–146.
22 K. Sayama, A. Nomura, T. Arai, T. Sugita, R. Abe, M. Yanagida, T. Oi, Y. Iwasaki, Y. Abe and H. Sugihara, *J. Phys. Chem. B*, 2006, **110**, 11352–11360.
23 A. Kudo, K. Ueda, H. Kato and I. Mikami, *Catal.Lett.*, 1998, **53**, 229–230.
24 B. Cao, J. Peng and Y. Y. Xu, *J. Cluster Sci.*, 2013, **24**, 771–785.
25 L. Zhang, G. Tan, S. Wei, H. Ren, A. Xia and Y. Luo, *Ceram. Int.*, 2013, **39**, 8597–8604.
26 Y. Hu, D. Li, Y. Zheng, W. Chen, Y. He, Y. Shao, X. Fu and G. Xiao, *Appl. Catal., B*, 2011, **104**, 30–36.
27 G. Long, F. Fresno, S. Grosss and U. L. Stangar, *Environ. Sci. Pollut. Res. Int.*, 2014, **21**, 11189–11197.
28 R. Rahimi, S. Zargari and M. M. Moghaddas, *Adv. Mater. Res.*, 2013, **702**, 172–175.
29 M. Xie, X. Fu, L. Jing, P. Luan, Y. Feng and H. Fu, *Adv. Energy Mater.*, 2014, **4**, 130095.
30 S. Ho-Kimur, S. J. A. Moniz, A. D. Handoko and J. W. Tang, *J. Mater. Chem. A*, 2014, **2**, 3948–3953.
31 S. Obregon and G. Colon, *RSC Adv.*, 2014, **4**, 6820–6926.
32 T. Y. Huo, X. F. Zhang, X. Dong, X. X. Zhang, C. Ma, G. W. Wang, H. C. Ma and M. Xue, *J. Mater. Chem. A*, 2014, **2**, 17366–17370.
33 H. Q. Jiang, H. Endo, H. Natori, M. Nagai and K. Kobayashi, *Mater. Res. Bull.*, 2009, **44**, 700–706.
34 M. Zhou, J. Bao, Y. Xu, J. J. Zhang, J. F. Xie, M. L. Guan, C. L. Wang, L. Y. Web, Y. Lei and Y. Xie, *ACS Nano*, 2014, **8**, 7088–7098.
35 M. Wu, Y. Li, Z. Deng and B. L. Su, *ChemSusChem*, 2011, **4**, 1481.
36 X. Zheng, S. Meng, J. Chen, J. Wang, J. Xian, Y. Shao, X. Fu and D. Li, *J. Phys. Chem. C*, 2013, **177**, 21263–21273.
37 C. W. Cheng, S. K. Karuturi, L. J. Liu, J. P. Liu, H. X. Li, L. T. Su, A. I. Y. Tok and H. J. Fan, *Small*, 2012, **8**, 37–42.
38 J. Liu, Y. Li, H. W. Huang, C. Wang, M. Wu, L. H. Chen and B. L. Su, *J. Mater. Chem. A*, 2014, **2**, 5051.
39 M. Wu, J. Jing, J. Liu, Z. Deng, Y. Li, O. Deparis and B. L. Su, *J. Mater. Chem. A*, 2013, **1**, 15491.
40 M. Wu, J. Liu, J. Jing, C. Wang, S. Z. Huang, Z. Deng, Y. Li and B. L. Su, *Appl. Catal., B*, 2014, **411**, 150–151.
41 X. Chen, J. Ye, S. Ouyang, T. Kako, Z. Li and Z. Zou, *J. Am. Chem. Soc.*, 2011, **5**, 4310–4318.
42 L. I. Halaoui, N. M. Abrams and T. E. Mallouk, *J. Phys. Chem. B*, 2005, **109**, 6334–6342.
43 P. R. Somani, C. Dionigi, M. Murgia, D. Palles, P. Nozar and G. Ruani, *Sol. Energy Mater. Sol. Cells*, 2005, **87**, 513–519.

44 C. L. Huisman, J. Schoonman and A. Goossens, *Sol. Energy Mater. Sol. Cells*, 2005, **85**, 115–124.
45 I. Rodriguez, F. Ramiro-Manzano, P. Atienzar, J. M. Martinez, F. Meseguer, H. Garcia and A. Corma, *J. Mater. Chem.*, 2007, **17**, 3205–3209.
46 S. Nishimura, N. Abrams, B. A. Lewis, L. I. Halaoui, T. E. Mallouk, K. D. Benkstein, J. van de Lagemaat and A. Frank, *J. Am. Chem. Soc.*, 2003, **125**, 6306–6310.
47 J. I. L. Chen, E. Loso, N. Ebrahim and G. A. Ozin, *J. Am. Chem. Soc.*, 2008, **130**, 5420–5421.
48 J. I. L. Chen, G. von Freymann, S. Y. Choi, V. Kitaev and G. A. Ozin, *Adv. Mater.*, 2006, **18**, 1915–1919.
49 J. I. L. Chen, G. von Freymann, V. Kitaev and G. A. Ozin, *J. Am. Chem. Soc.*, 2007, **129**, 1196–1202.
50 M. Wu, A. Zheng, F. Deng and B. L. Su, *Appl. Catal., B*, 2013, **138– 139**, 219–228.
51 L. Dong, S. Guo, S. Zhu, D. Xu, L. Zhang, M. Huo and X. Yang, *Catal. Commun.*, 2011, **16**, 250–254.
52 Y. Guo, X. Yang, F. Ma, K. Li, L. Xu, X. Yuan and Y. Guo, *Appl. Surf. Sci.*, 2010, **256**, 2215–2222.
53 N. Myung, S. Ham, S. Choi, Y. Chae, W. Kim, Y. J. Jeon, K. Paeng, W. Chanmanee, N. R. de Tacconi and K. Rajeshwar, *J. Phys. Chem. C*, 2011, **115**, 7793–7800.
54 Z. Ozlem Kocabaş-Ataklı and Y. Yurum, *J. Chem. Eng.*, 2013, **225**, 625–635.
55 Z. F. Bian, J. Zhu, S. H. Wang, Y. Cao, X. F. Qian and H. X. Li, *J. Phys. Chem. C*, 2008, **112**, 6258–6262.
56 Y. Q. Wu, G. X. Lu and S. B. Li, *J. Phys. Chem. C*, 2009, **113**, 9950–9955.
57 A. Zhang and J. Zhang, *Mater. Lett.*, 2009, **63**, 1939–1942.
58 L. D. Zhang and C. M. Mo, *Nanostruct. Mater.*, 1995, **6**, 831–834.
59 L. Q. Jing, X. J. Sun, B. F. Xin, B. Q. Wang, W. M. Cai and H. G. Fu, *J. Solid State Chem.*, 2004, **177**, 3375–3382.
60 J. Cao, B. Luo, H. Lin, B. Xu and S. Chen, *Appl. Catal., B*, 2012, **111–112**, 288–296.
61 Z. Xiong, L. L. Zhang, J. Ma and X. S. Zhao, *Chem. Commun.*, 2010, **46**, 6011–6099.
62 J. Su, L. Guo, N. Bao and C. A. Grimes, *Nano Lett.*, 2011, **11**, 1928–1933.
63 A. Hagfeldt and M. Gratzel, *Chem. Rev.*, 1995, **95**, 49–68.
64 K. Sayama, A. Nomura, T. Arai, T. Sugita, R. Abe, M. Yanagida, T. Oi, Y. Iwasaki, Y. Abe and H. Sugihara, *J. Phys. Chem. B*, 2006, **110**, 11352–11360.
65 S. Lee, D. H. Kim and J. H. Moon, *ACS Appl. Mater. Interfaces*, 2013, **5**, 12526–12532.

